A New Method of Calculating Ocean Temperatures Using Expendable Bathythermographs

John Abraham (Corresponding author), John Gorman

School of Engineering, University of St. Thomas

2115 Summit Ave, St. Paul, MN 55105-1079, USA

Tel: 1-651-962-5766   E-mail: jpabraham@stthomas.edu

Franco Reseghetti

ENEA, UTMAR-OSS, Forte S. Teresa, 19032 Pozzuolo di Lerici, Italy

Kevin Trenberth

National Center for Atmospheric Research, P.O. Box 3000, Boulder, CO 80307, USA

W. J. Minkowycz

Department of Mechanical and Industrial Engineering, University of Illinois at Chicago

Chicago, IL 60607, USA

Abstract

A newly developed method is proposed to simplify the measurement of ocean temperatures and heat content. That method, which makes use of expendable bathythermograph probes (XBTs), is able to account for variations in the probes such as weight, size, drop height, and wire length. Additionally, this new method accounts for variations in the conditions of the drop region, such as ocean temperature and salinity. The method requires the determination of the drag coefficient which corresponds to the probe's travel through water. This coefficient is introduced into a dynamic equation in which the position of the probe is calculated at a sequence of time steps. The calculated depths are matched with corresponding local temperatures to enable a determination of ocean heat content. The method outlined here avoids the reliance upon experimental correlations which are traditionally used for ocean-temperature measurements. To validate the method, it was applied to two calibrated XBT experiments. It is shown that the new method provides results that are virtually identical with results obtained from industry-standard techniques, and it is possible that the method can be applied to historical archives.

Keywords: Global warming, Ocean heat content, Expendable bathythermographs, Ocean temperatures, Drag coefficients

1. Introduction

The world's oceans are enormous thermal reservoirs that respond slowly to perturbations in the Earth's energy budget. Their thermal inertia allows them to absorb large amounts of thermal energy during times when the planet is in a net radiation imbalance, such as it is now.

Tracking the flow of energy within the Earth's atmosphere and oceans requires measurements with sufficient resolution to detect small changes in temperature. For ocean monitoring, a number of techniques are commonly used. These techniques have evolved over time and have become more accurate, at the same time, their global distribution has increased.

Measurements are made at the top-of-atmosphere (TOA) of the incoming and outgoing radiation from Earth. While the planetary imbalance at TOA is too small to measure directly from satellite, instruments are far more

stable than they are absolutely accurate with calibration stability < 0.3 Wm^{-2} per decade (95% confidence) (Loeb *et al*., 2009). Tracking relative changes in Earth's energy by measuring solar radiation in and infrared radiation out to space, and thus changes in the net radiation, seems to be at hand (Wong *et al*., 2009). However, assessing all evidence together suggests that with global warming, the imbalance is positive and estimated to be 0.9±0.5 W m^{-2} (Trenberth *et al*., 2009).

The challenge then is to perform an inventory of all the places where the surplus energy is being deposited (Trenberth and Fasullo, 2010). Over 90% of the energy uptake has been in the ocean (Bindoff *et al*., 2007; Trenberth, 2009). Commonly, ocean temperature measurements, and consequently heat-content measurements, are made with devices that are released into the ocean waters. Among the devices are expendable bathythermographs (XBTs), conductivity/temperature/depth probes (CTDs), and Argo floats/gliders. Each of these devices contains a temperature-sensing instrument and a means to transmit temperature information to a data collection device. Indeed recent analyses of ocean-heat content (OHC) (Lyman *et al*., 2010) show clearly that the ocean is warming but the uncertainty among many estimates is substantial and arises from the XBT correction methodology more than anything else.

The XBT device is the oldest, and most numerous (millions of profiles) of these measuring devices. The XBTs were initially employed by navies to determine the depth of the thermocline, but more recently, were adopted for climatological studies as researchers began to use the information gathered from XBT experiments to assess the changes in OHC.

During an XBT experiment (drop), the device is jettisoned from a position of approximately 2.5 meters above the ocean surface. It falls through the ocean at a rate of approximately 6.5 m/s but which varies slightly, depending on the local water temperature and salinity, and on the details of the device. During its descent, the XBT unwinds a thin copper wire which trails the probe. This copper wire is connected to a data collection system onboard a ship and it is through this wire that temperature information is transmitted.

The temperature of the water column is sensed by an NTC thermistor housed in the nose of the probe. The thermistor has a time constant of 0.1 seconds. Electronics sample data at 10 Hz and a time-resistance map is obtained. The XBT does not measure depth directly; software calculates depth-temperature pairs through a polynomial fall rate question (FRE) having the general form

$$depth\,(t) = \; a + bt + ct^2 + dt^3 \qquad\qquad (1)$$

The manufacturer (LM Sippican) and many researchers analyzing XBT data assumed the coefficients to be constant and $a=d=0$. The *b* term represents the speed of the probes when it touches the seawater surface whereas *c* describes the changes in the mass and water properties. There are a number of different XBT probe variants depending on their maximum depth (T4/T6/T7/DB class, T5 class, T10 class, etc.) Each class uses its own fall-rate coefficients which are originally supplied by the manufacturer.

The uncertainty described by LM Sippican was 5 m or 2% of depth, whichever is greater and 0.2 ^{o}C on temperature (including coupling between the recording system and probes). These uncertainties are independent of the XBT class. Uncertainty in the depth of an XBT can lead to errors in ocean temperature calculations. A number of studies have been completed related to the impact of systematic FRE biases to ocean heat content calculations (Levitus *et al*., 2005; Wijffels el al., 2008; Gouretski and Koltermann, 2007; Ishii and Kimoto, 2009; and Levitus *et al*., 2009).

Biases in the various XBT fall-rate equations have been identified by contemporaneous and collocated measurements with other devices since the 1970s, primarily CTD devices which are taken to be the standard against which the XBT is compared. Comparisons between the devices allow quantification of XBT errors (Seaver and Kuleshov, 1982; Heinmiller *et al*., 1983; Hanawa and Yoritaka, 1987; and Prater, 1991). Each class of XBT device is accompanied with a FRE from the manufacturer. However, various researchers have proposed alternative values for the coefficients in the FREs (Hanawa *et al*., 1995; Boyd, 1993; and Kizu, 2005). Among them, the values calculated by Hanawa *et al*. (1995) have been treated as standard for the T4/T6/T7/DB class and are accepted by the manufacturers.

There are a number of issues which complicate the universal use of FREs. First, the determination of an FRE depends on the location of the comparison experiments. For example, the rate of descent of an XBT will depend on the temperature and salinity of the ocean water through which it falls. When XBT drops occur in colder, more viscous waters, it is expected that the rate of descent will be lower than it would be for an equivalent release in tropical waters; such an effect is not incorporated into the FREs. Additionally, there is instrument-to-instrument variation for both CTD and XBT devices themselves which make the unambiguous determination of an FRE

difficult (Boyer *et al*., 2011). Thirdly, ocean temperature distributions change in time, often in hours. As a result, CTD-XBT releases which are considered contemporaneous are, in fact, separated by enough time and are unlikely to be in exactly the same location, so that a comparison is difficult. For these reasons, an alternative approach is set forth here. This new approach will not rely upon an experimentally determined FRE. Rather, calculations of XBT depths will be based on a dynamic model of the forces acting on an XBT during its descent. Those forces include weight, buoyancy, and drag, all of which change in time. Buoyancy and weight forces evolve during descent because the probe unspools a copper wire which is used to transmit temperature data to the ship. Drag forces also change because of variations in the viscosity of the water and because of the changes in the probe velocity.

The analysis presented here is focused on the T4/T6/T7/DB class of XBT devices however the technique can be applied to other XBT classes as well.

2. Dynamic Model

The model set forth here is that recently disclosed in Stark *et al*., (2011).That publication limited its study to the T5 XBT model. It is based on an unsteady balance of forces and changes in momentum of the probe during its descent. That balance is expressed as

$$F_{net} = F_{buoy} - F_{drag} = \frac{d(m_p V)}{dt} = m_p \frac{d(V)}{dt} + V \frac{d(m_p)}{dt} \tag{2}$$

The buoyancy and drag forces are represented by F_{buoy} and F_{drag}, respectively; the probe mass is indicated by m_p. It should be noted that the dynamic model includes changes in the probe mass which result from the unspooling wire during descent. The two primary forces can be represented by

$$F_{buoy} = (m_p - m_w)g \tag{3}$$

and

$$F_{drag} = C_d \frac{1}{2} \rho V^2 A \tag{4}$$

Here, the subscript *w* refers to water properties, C_d is the drag coefficient, ρ, V, and A are the water density, probe velocity, and probe frontal area, respectively. If Eqs. (2)- (4) are combined, and if Eq. (2) is expressed in a finite-different form using a forward-stepping algorithm, it is possible to obtain

$$V^{new} = V + \frac{\Delta t}{m_p} \left[(m_p - m_w)g - C_d \frac{1}{2} \rho V^2 A - V^2 \frac{dm_p}{dx} \right] \tag{5}$$

2.1 Determination of drag coefficients

This model allows the calculation of velocity at a new time step provided that information at the present time step is known. One key term on the right-hand side of Eq. (5) is the value of the drag coefficient. Traditionally, drag coefficients for XBT devices have been estimated using experiments on similar shaped devices (Green, 1984; Hallock and Teague, 1992). While these works used admittedly crude estimates of the drag coefficients, they were based on the best available information at the time. With the advent of highly accurate computational fluid dynamic analysis, it is possible to calculate drag coefficients with higher fidelity (Stark *et al*., 2011).

The new computational method requires that the fluid region surrounding the probe be subdivided into grid regions called elements. At each element, the fluid motion is solved by conserving fluid momentum and mass. The conservation of mass and momentum equations are expressed, respectively, as

$$\frac{\partial u_i}{\partial x_i} = 0 \tag{6}$$

and

$$\rho \left(u_i \frac{\partial u_j}{\partial x_i} \right) = -\frac{\partial p}{\partial x_i} + \frac{\partial}{\partial x_i} \left((\mu + \mu_{turb}) \frac{\partial u_j}{\partial x_i} \right) \quad j = 1,2,3 \tag{7}$$

The μ terms represent the viscosity of the fluid, and the *u* terms are velocities in one of three coordinate directions. The equations are presented in tensor form for compactness. The solution of Eqs. (6) and (7) require

that turbulence be incorporated into the model. Turbulence was dealt with by use of the Shear Stress Transport (SST) turbulence model which was initially proposed by Menter (1994). Additionally, the present method incorporates a modification to the SST turbulence model which accounts for laminar-to-turbulent transition. Such transition typically occurs in fluid which flows over blunt objects. At the leading edge of a blunt object, the flow is likely to be laminar. Further downstream however, the flow may transition to a turbulent state as the boundary layer thickness increases. It is often important to account for transition because it affects the drag forces. Transition was dealt with here using a transitional model (Menter *et al.*, 2002; Menter *et al.*, 2004a; Menter *et al.*, 2004b). Both the standard turbulence model and the transitional modification will be employed in the present investigation. Results from the two approaches will be compared with each other and with expected values of the drag coefficient.

The transition model has been widely adopted for a number of fluid flow situations including steady and unsteady flows, internal and external flows, flows in regions of changing cross section, and flows across blunt objects (Abraham, *et al.*, 2008; Abraham and Thomas, 2009; Abraham, *et al.*, 2009; Abraham, *et al.*, 2010; Gorman, *et al.*, 2010; Lovik *et al.*, 2009; Minkowycz *et al.*, 2009; Sparrow *et al.*, 2009; Thomas and Abraham, 2010). An image of a typical computational mesh is shown in Figure 1 where fine elements are seen arranged along the probe surfaces.

The boundaries were placed sufficiently far from the probe body so that their position did not affect the results. In total, more than 2 million elements were used and a mesh-independency test was performed to ensure that the results were independent of the mesh. At the inlet surface, a relative velocity of the water was provided, and it was assumed that this velocity was aligned with the probe body. A turbulence intensity of 5% was specified there as well. More details of the simulation method are provided in Stark *et al.* (2011) where calculations were first performed on an XBT T5 class probe. In this report, the probe was treated as falling without rotating. In practice, the probe fins are canted to induce a rotation that helps unspool the copper wire. Future simulations will be directed toward incorporating the impact of rotation on drag.

3. Results and Discussion

3.1 Fluid pressure and surface friction

The computations provide information about all fluid properties throughout the flow regime and at the probe surface. Among the important quantities are the velocity and pressure of the fluid and the surface stress and surface pressure which exist on the probe exterior. To elucidate some of the fluid results, Figure 2 shows that there is a high-pressure region at the leading edge of the probe. The probe contains a through-flow channel that allows some fluid to pass through the center of the probe body. That channel contains the temperature measurement equipment which is located near the channel inlet. At the inlet of the channel, there is a continuation of the high-pressure zone which dissipates as fluid passes further downstream. On the downstream side of the probe, the pressure is notable lower than in the upstream region. The different upstream and downstream pressures are the source of pressure drag on the object, which is the primary source of drag forces.

Shear stresses of the fluid on the surface of the probe (Figure 3) reveal that the shear stress is low at the leading and trailing edges of the probe but takes on higher values on the forward part of the probe mid-body. Also of note are the low magnitudes of the shear stress compared with the pressures exhibited in Figure 2 confirming the expectation that pressure drag is more significant that frictional drag on the probes. The details of the shear stress and pressure drag vary slightly according to the probe's instantaneous velocity and according to the probe class. However, these variations are only slight and the images in Figures 2 and 3 can be considered representative of all probes.

3.2 Probe drag coefficients

The most important outcome from the fluid flow simulations is the determination of the drag coefficient. That quantity is dependent on the dimensional group called the Reynolds number, which accounts for the probe velocity, water viscosity, and probe dimensions. According to fluid-flow theory, the drag coefficient should depend uniquely on the value of the Reynolds number. The fluid dynamic simulations allowed a determination of the drag force on the probe and, through Eq. (4), a determination of the drag coefficient. The results for drag are shown for models with and without transition in Figure 4. There, values are compared with those from Green (1984) which were based on generic streamlined objects. It can be seen that the SST model (without transition), overpredicts the drag coefficients with respect to the Green results. On the other hand, the model with transition underpredicts drag. The differences in the two results are likely due to the separation which occurs on the downstream faces of the XBT device. The SST model is more capable of predicting the onset of flow separation than is the transitional model. This difference leads to the varying drag forces. It is also possible that the seam

between the XBT nose cone and the main body promotes a premature transition to full turbulence. Of the two results, depth calculations using the SST approach were more closely aligned with collocated CTD experiments. Consequently, those results are adopted here, and the corresponding drag coefficient correlation is

$$C_d = 2.18 \times 10^{-15} \cdot Re^2 - 1.10 \times 10^{-8} \cdot Re + 0.140 \qquad (8)$$

3.3 Probe depth calculations

The final step in the analysis is the application of the method set forth in Eq. (5) with the drag coefficients which are displayed in Figure 4. It was decided to apply the method to recent XBT experiments which were contemporaneous with CTD drops. Such a comparison allows for an independent assessment of the quality of the new method. During the experiments, results from the CTD probe were considered very accurate, because of their greater depth control. The industry-accepted FRE was employed which utilized values of coefficients from Eq. (1) that are; a = d = 0, b = -0.00225, and c = 6.691. These coefficients calculate a fall depth in meters for a release time measured in seconds.

The comparison data for the first CTD-XBT experiment (Figure 5) reveals that there is an excellent visual agreement between the results. The data are only shown for 100 m in order to accentuate small differences in the records. The corresponding results from a second experiment (Figure 6) again reveal that there is excellent agreement between both the industry-standard FRE and the present dynamic model. It is noted that the differences between the CTD and the XBT temperatures are somewhat larger in Figure 6 compared with Figure 5, particularly in the 10-20 m depth range. Part of this difference can be explained by the fact that the probes were released with a larger separation in time. Experiments have shown that ocean temperature pattern can vary by the magnitude shown in the figure over such short time spans.

A quantitative method of assessing the quality of the new method is to compare calculated mass-average temperatures with those obtained using the industry-standard FRE. Calculations of the mass-average temperature are made by integrating the product of local temperature and mass during the probe descent. Mathematically, this process is

$$T_{bulk} = \frac{1}{m} \int_0^d T dm \qquad (9)$$

Which is carried out from the surface (x = 0) to some depth *d*. The determination of the bulk temperature is completed numerically by transforming Eq. (9) to a numerical form as

$$T_{bulk} = \frac{\sum T_i \Delta m_i}{\sum \Delta m_i} \qquad (10)$$

Where the subscript refers to the ith depth level in the ocean. With this technique, it is possible to calculate bulk temperature values from the ocean surface to any arbitrary depth. In the oceanographic community, other temperature definitions are commonly employed for various purposes. For instance, the potential temperature is often used for ocean heat content measurements. The potential temperature is defined as the temperature that water would have if it were raised adiabatically to the ocean surface. For the purposes of demonstration however, the use of the bulk temperature is appropriate.

To illustrate the technique, experimental data from Figures 5 and 6 are employed. The results (Table 1) are segregated into two parts corresponding to the two experiments. For each case, temperatures are listed from the CTD probe and from the XBT device. For the XBT, temperatures have been found by means of the industry-standard FRE and by the present method. Deviations from the CTD results are listed in parentheses. It is seen that both XBT methods provide temperatures that are very close to the CTD values and are even more similar to those of the FRE. It should be noted that the sensor accuracy is stated to be +/- 0.01 ^{o}C.

These results suggest that a dynamic model with the drag coefficient relationship given in Eq. (8) can be used to predict the depth of an XBT device falling through a water column. The method allows experimenters to make corrections for changes in the operating conditions (such as drop height), the probe dimensions, and the wire diameter and length. Additionally, because the technique uses temperature information gathered during its descent to continually update the model, it automatically deals with variations in water temperature which enables it to be used in more diverse environments than the standard FRE approach.

4. Concluding Remarks

In this work, a new method has been set forth which allows the determination of the depth of XBT probes for

climatology studies. The new method is based on a dynamic model of an XBT probe which includes drag, buoyancy, and inertia; the new method is able to be used independent of a fall-rate equation (FRE). One advantage of the new method is that it functions regardless of the local conditions, such as water temperature. The critical step which allows this method is that drag coefficients have been determined as a function of Reynolds number. To the best knowledge of the authors, this approach is the first exposition of numerically determined drag-coefficient information for oceanographic probes.

The new method has been applied to the T4/T6/T7/DB class of XBT probes. Results are compared with near simultaneous releases of CTD devices which are considered exact. It has been shown that the new method is able to calculate ocean temperatures with accuracies that are sufficiently appealing to justify its continued use. Next stages of the work include incorporating probe rotation in the simulations. Additionally, it will be possible to analyze archival XBT data to re-assess ocean heat content.

References

Abraham, J. P, Tong, J. C. K., & Sparrow, E. M. (2008). Breakdown of laminar pipe flow into transitional intermittency and subsequent attainment of fully developed intermittent or turbulent flow. *Numerical Heat Transfer*, 54, 103-115. http://dx.doi.10.1080/10407790802156178.

Abraham, J. P., & Thomas, A. P. (2009). Induced co-flow and laminar-to-turbulenttransition with synthetic jets. *Computers and Fluids*, 38, 1011-1017. http://dx.doi.10.1016/j.compfluid.2008.01.028.

Abraham, J. P., Sparrow, E. M., & Tong, J. C. K. (2009). Heat transfer in all pipe flow regimes - laminar, transitional/intermittent, and turbulent. *Int. J. Heat Mass Tran.,* 52, 557-563. http://dx.doi.10.1016/j.ijheatmasstra nsfer.2008.07.009.

Abraham, J. P., Sparrow, E. M., Tong, J. C. K., *et al*. (2010). Internal flows which transist from turbulent through intermittent to laminar. *Int. J. Therm. Sci.*, 49, 256-263. http://dx.doi.10.1016/j.ijthermalsci.200 9.07.013.

Bindoff, N. L., *et al*. (2007). Observations: oceanic climate change and sea level. In S. Solomon *et al*. (Ed.), *Climate Change 2007: The Physical Science Basis. Contrib. Working Group I Fourth Assessment Report of the IPCC,*Cambridge Univ. Press, Cambridge, U.K., 385-428.

Boyd, J. (1993).The temperature and depth accuracy of Sippican T-5 XBTs. *J. Atmos. Ocean Tech*., 10, 128-139. http://dx.doi.org/10.1175/1520-0426(1993)010<0128:TTADAO>2.0.CO;2

Boyer, T., *et al*. (2011). Investigation of XBT and XCTD biases in the Arabian Sea and the Bay of Bengal with implications for climate studies. *J. Atmospheric and Oceanic Technology*, 28, 266-286. http://dx.doi.org/10.1175/2010JTECHO784.1

Gorman, J. M., Sherrill, N. K., & Abraham, J. P. (2010). Analysis of drag-reducing techniques for olympicskeleton helmets. *ANSYS Users Conference*, Minneapolis, MN.

Gouretski, V., & Koltermann, K. (2007). How much is the ocean really warming? *Geophys. Res. Lett*., 34, L01610. http://dx.doi.10.1029/2006GL027834.

Green, A. (1984). Bulk dynamics of the expendable bathythermograph. *Deep-Sea Research*, 31, 415-426. http://dx.doi.10.1016/0198-0149(84)90093-1.

Hallock, Z., & Teague, W. (1992). The fall rate of the T-7 XBT. *J. Atmos. Ocean Tech*., 9, 470-483. http://dx.doi.org/10.1175/1520-0426(1992)009<0470:TFROTT>2.0.CO;2

Hanawa, K., & Yoritaka, H. (1987). Detection of systematic errors in XBT data and their correction. *J. Ocean. Soc. Japan*, 43, 68-76. http://dx.doi.10.1007/BF02110635.

Hanawa, K., *et al*. (1995). A new depth-time equation for Sippican or TSKT-7; T-6; and T-4 expendable bathythermographs (XBT). *Deep-Sea Research*, 42, 1423-1451. http://dx.doi.10.1016/0967-0637(95)97154-Z.

Heinmiller R., *et al*. (1983). Systematic errors in expendable bathythermograph (XBT) profiles. *Deep-Sea Res.,* 30, 1185-1197. http://dx.doi.10.1016/0198-0149(83)90096-1.

Ishii, M., & Kimoto, M. (2009). Reevaluation of historical ocean heat content variations with an XBT depth bias correction. *J. Oceanogr*. 65, 287-299. http://dx.doi.10.1007/s10872-009-0027-7.

Kizu, S., Yoritaka, H., & Hanawa, K. (2005). A new fall-rate equation for T-5 expendable bathythermograph (XBT) by TSK. *J. Oceanography*, 61, 115-121. http://dx.doi.10.1007/s10872-005-0024-4.

Levitus, S. (2009). Global ocean heat content 1955-2008 in light of recently revealed instrumentation problems.

Geophys. Res. Lett., 36, L07608. http://dx.doi.10.1029/2008GL037155.

Levitus, S., Antonov, J., & Boyer, T. (2005). Warming of the world ocean. *Geophys. Res. Lett.*, 32, L12602. http://dx.doi.10.1126/science.2887.5461.2225.

Loeb, N. G., *et al.*, (2009). Towards optimal closure of the Earth's top-of-atmosphere radiation budget. *J. Climate*, 22, 748-766. http://dx.doi.10.1175/2008JCLI2637.1

Lovik, R. D., Abraham, J. P., Minkowycz, W. J., & Sparrow, E. M. (2009). Laminarization and turbulentization in a pulsatile pipe flow. *Numerical Heat Transfer A*, 56, 861-879. http://dx.doi.10.1018/10407780903466568.

Lyman, J. M., *et al.* (2010). Robust warming of the global upper ocean. *Nature*, 465, 334-337. http://dx.doi.10.1038/nature09043.

Menter, F. (1994). Two equation eddy-viscosity models for engineering applications. *AIAA J.*, 32, 1598-1605. http://dx.doi.org/10.2514/3.12149

Menter, F., Esch, T., & Kubacki, S. (2002). Transition modelling based on local variables. *5th Int. Symposium on Engineering Turbulence Modeling and Measurements*, Mallorca, Spain.

Menter, F., *et al*. (2004a). A correlation–based transition model using local variables, part I – model formulation. *Proceedings of ASME Turbo Expo Power for Land, Sea, and Air*, Vienna, Austria

Menter, F., *et al*. (2004b). A correlation –based transition model using local variables, part II – test cases and industrial applications. *Proceedings of ASME Turbo Expo Power for Land, Sea, and Air*, Vienna, Austria

Minkowycz, W. J., Abraham, J. P., & Sparrow, E. M. (2009). Numerical simulation of laminar breakdown and subsequent intermittent and turbulent flow in parallel plate channels:effects of inlet velocity profile and turbulence intensity. *Int. J. Heat Mass Transfer*, 52, 4040-4046. http://dx.doi.10.1016/j.ijheatmasstransfer.2009.03.041.

Prater, M. (1991). A method for depth and temperature correction of expendable probes. *J. Atmos. Ocean Tech.*, 8, 888-894. http://dx.doi.org/10.1175/1520-0426(1991)008<0888:AMFDAT>2.0.CO;2

Seaver, G., & Kuleshov, S. (1983). Experimental and analytical error of the expendable baththermograph. *J. Phys. Oceanography*, 12, 592-600. http://dx.doi.org/10.1175/1520-0485(1982)012<0592:EAAEOT>2.0.CO;2

Sparrow, E. M., Abraham, J. P., & Minkowycz, W. J. (2009). Flow separation in a diverging conical duct: effect of reynolds number and divergence angle. *Int. J Heat Mass Transfer*, 52, 3079-3083. http://dx.doi.10.1016/j.ijheatmasstransfer.2009.02.2010.

Stark, J. R., Gorman, J. M., Hennessey, M. P., Reseghetti, F., Willis, J., Lyman, J., & Abraham, J. P. (2011). A computational method for determining XBT depths. *Ocean Sciences*, 7, 733-743. http://dx.doi.10.5194/osd-8-17 77-2011.

Thomas, A. P., & Abraham, J. P. (2010). Sawtoothvortex generators for underwater propulsion. *Open Mech. Eng.*, 4, 1-7. http://dx.doi.org/10.2174/1874155X01004010001

Trenberth, K. E. (2009). An imperative for adapting to climate change: tracking earth's global energy. *Current Opinion Env. Sustainability*, 1, 19-27. http://dx.doi.10.1016/j.cosust.2009.06.001.

Trenberth, K. E., & Fasullo, J. T. (2010). Tracking Earth's energy. *Science*, 328, 316-317. http://dx.doi.10.1126/science.1187272.

Trenberth, K. E., Fasullo, J. T. & Kiehl, J. (2009). Earth's global energy budget. *Bull. Amer. Meteor. Soc.*, 90, 311-323. http://dx.doi.org/10.1175/2008BAMS2634.1

Wijffels S., *et al*. (2008). Changing expendable bathythermograph fall rates and their impact onestimates of thermostericsea rise. *J. Climate*, 21, 5657-5672. http://dx.doi.10.1175/2008JCLI2290.1

Wong, T., Stackhouse, P. W. Kratz, D. P., and Wilber, A. C. (2009). Earth radiation budget at top-of-atmosphere. *Bull. Amer. Meteor. Soc.*, 90, S33-S34.

Table 1. Comparison of XBT temperatures with results from CTD probes, all temperatures in ^{o}C

Depth used in calculation	CTD bulk temperature	XBT temperature using FRE	XBT temperature with present method
Experiment 1			
100	14.69	14.72 (0.03)	14.74 (0.05)
200	14.34	14.35 (0.01)	14.36 (0.02)
Experiment 2			
100	14.40	14.29 (0.11)	14.29 (0.11)
200	14.22	14.17 (0.05)	14.17 (0.05)
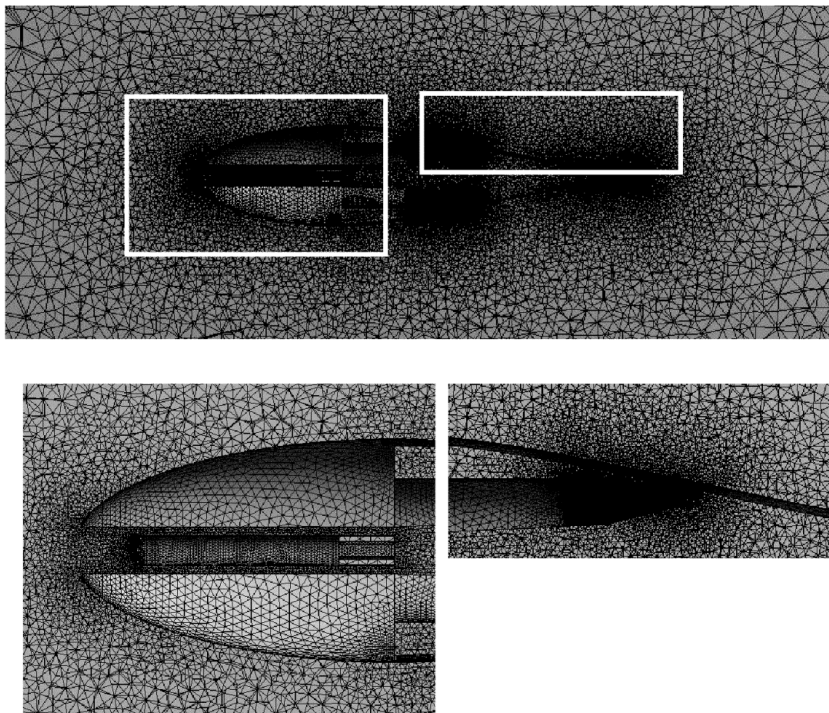
Figure 1. Computational Mesh
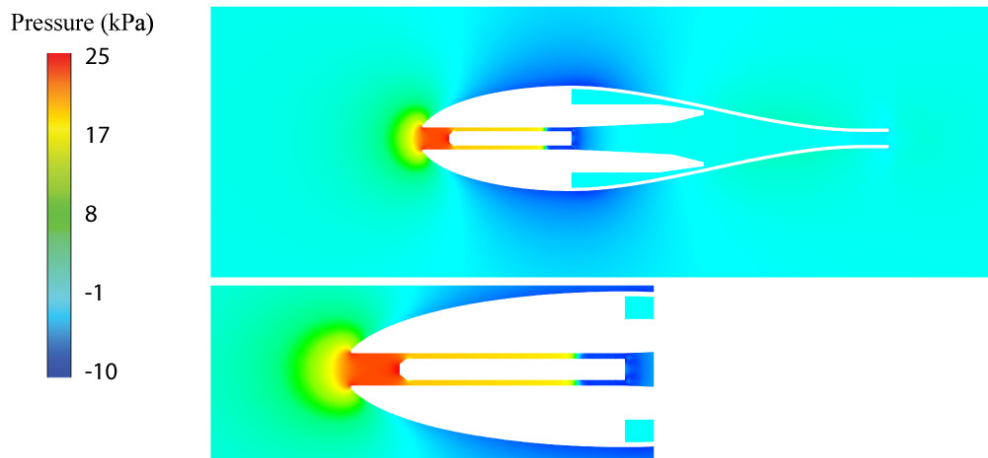
Figure 2. Pressure contour near the body of the probe
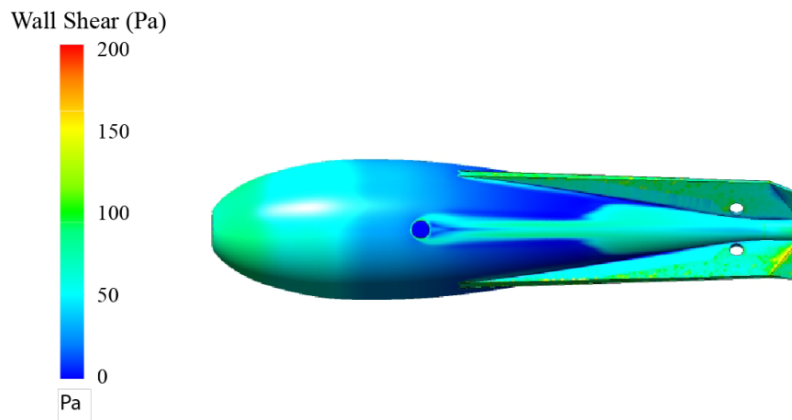
Figure 3. Shear stress on probe surface
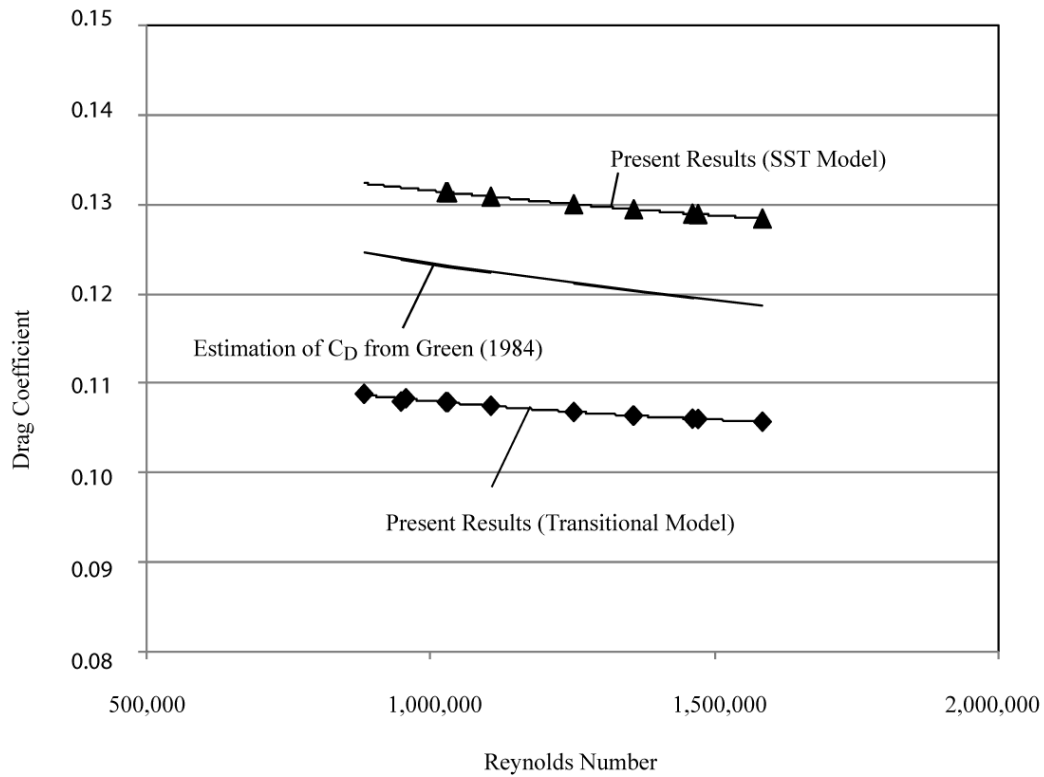
Figure 4. T7 Probe Drag Coefficient
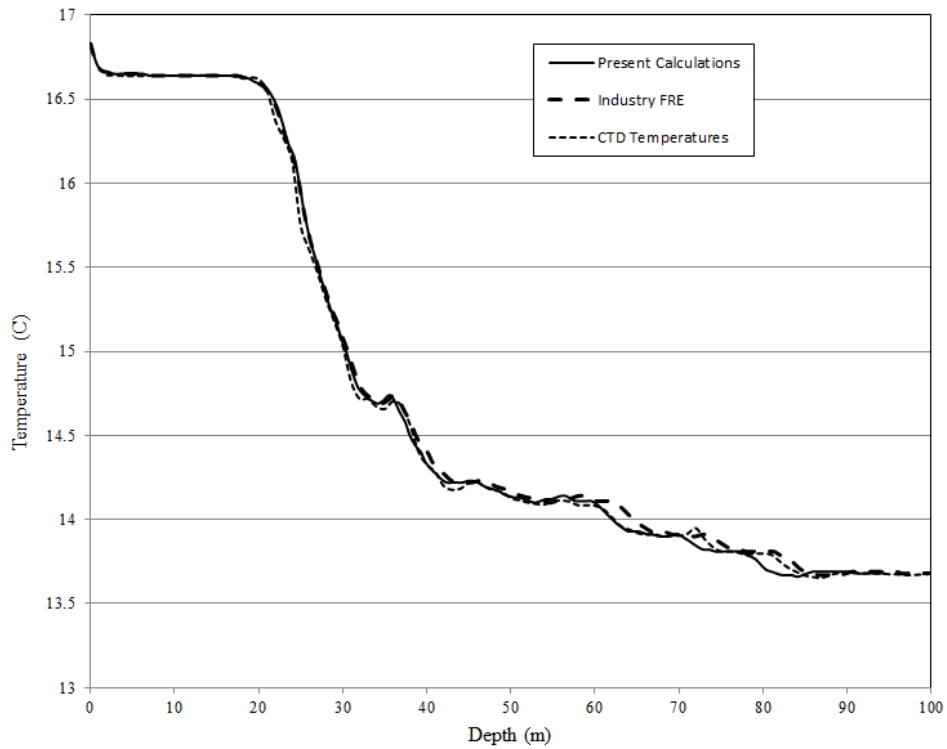
Figure 5. Comparisons of the new XBT method and the industry-standard method with contemporaneous CTD data, experiment 1
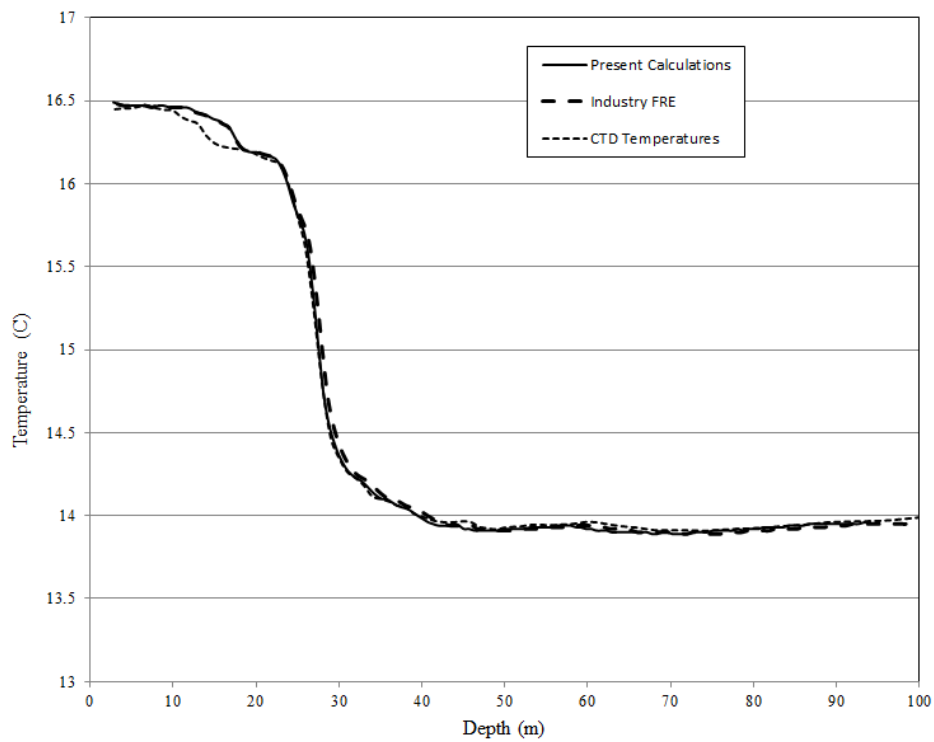
Figure 6. Comparisons of the new XBT method and the industry-standard method with contemporaneous CTD data, experiment 2